Acta Oceanol. Sin., 2014, Vol. 33, No. 12, P. 58–66
DOI: 10.1007/s13131-014-0572-9
http://www.hyxb.org.cn
E-mail: hyxbe@263.net

Pourbaix diagrams to decipher precipitation conditions of Si-Fe-Mn-oxyhydroxides at the PACMANUS hydrothermal field

YANG Baoju[1,2], ZENG Zhigang[1]*, WANG Xiaoyuan[1], YIN Xuebo[1], CHEN Shuai[1]

[1] Seafloor Hydrothermal Activity Laboratory of the Key Laboratory of Marine Geology and Environment, Institute of Oceanology, Chinese Academy of Sciences, Qingdao 266071, China
[2] University of Chinese Academy of Sciences, Beijing 100049, China

Received 17 July 2013; accepted 26 March 2014

Abstract

Utilizing Si, Fe and Mn concentrations within the end-member PACMANUS hydrothermal fluid, Si-Fe-Mn-H_2O Pourbaix diagrams were constructed at 300°C and 25°C. The Pourbaix diagrams show that the main Si, Fe and Mn oxides species precipitating from the hydrothermal fluid were SiO_2, $Fe(OH)_3$, $Fe_3(OH)_8$, Mn_3O_4, and Mn_2O_3 at 25°C. During mixing of hydrothermal fluid with seawater, SiO_2 precipitated earlier than Fe-Mn-oxyhydroxides because of the lower stability boundary. Then $Fe(OH)_2$ precipitated first, followed by $Fe_3(OH)_8$ and $Fe(OH)_3$, and last, small amounts of Mn_3O_4 and Mn_2O_3 precipitated. $Fe(OH)_3$ was readily deposited in alkaline solution with little influence by Eh. There were many Si-Fe-Mn-concentric particles in the polished sections of the massive precipitates collected from PACMANUS. In the concentric nucleus and ellipsoid, Si oxides precipitated first before the hydrothermal fluid had mixed with seawater. In the concentric nucleus, after the precipitation of Si oxides, the increase of pH and Eh promoted the precipitation of Mn oxides around the Si oxides. In the large ellipsoid, the precipitation of Fe was divided into two periods. In the early period, increase of pH value of hydrothermal fluid produced by low-temperature convection and an input of a small volume of seawater promoted a small amount of $Fe(OH)_3$ to precipitate in the Si-rich core. In the late period, after complete mixing with seawater and the resultant fluid was close to neutral or slightly alkaline in pH, $Fe(OH)_3$ was easily precipitated from the solution and distributed around the Si-rich core.

Key words: Si-Fe-Mn-oxyhydroxides, PACMANUS hydrothermal field, Pourbaix diagrams

Citation: Yang Baoju, Zeng Zhigang, Wang Xiaoyuan, Yin Xuebo, Chen Shuai. 2014. Pourbaix diagrams to decipher precipitation conditions of Si-Fe-Mn-oxyhydroxides at the PACMANUS hydrothermal field. Acta Oceanologica Sinica, 33(12): 58–66, doi: 10.1007/s13131-014-0572-9

1 Introduction

Amorphous Fe- and Mn-oxyhydroxides and silica deposits are widely distributed on the seafloor of hydrothermal fields in various geological settings: mid-ocean ridges (Benjamin and Haymon, 2006; Dekov et al., 2010), back-arc basins (Iizasa et al., 1998; Hein et al., 2008; Sun et al., 2012; Zeng et al., 2012), and seamounts (Alt, 1988; Karl et al., 1989; Binns and Scott, 1993; Binns et al., 1993; Bogdanov et al., 1997; Emerson and Moyer, 2002; Edwards et al., 2011). Hydrothermal Fe-oxyhydroxides on the seafloor can be divided into three sources: oxidation products of hydrothermal sulfides, primary Fe-oxyhydroxide from hydrothermal fluid, and metalliferous sediments from hydrothermal plume fallout (Hekinian et al., 1993; Little et al., 2004). Mn oxides are generally of three types: hydrogenetic (precipitated from seawater), hydrothermal (precipitated from hydrothermal fluids), and diagenetic (precipitated in the sediment from pore fluids; Hein et al., 2008). Hydrothermal Si-Fe-Mn-oxyhydroxides are widely distributed at hydrothermal fields and are often used to decipher the dispersal patterns and evolution of hydrothermal fluid (Hrischeva and Scott, 2007). In addition, these deposits might be a helpful guidance for the exploration of ancient volcanogenic massive sulfides (Zeng et al., 2012).

The origin (Bonatti et al., 1972; Hekinian et al., 1993; Hein et al., 1994, 1997), element adsorption, and transport (Halbach, 1986; Takahashi et al., 2007) of Si-Fe-Mn-oxyhydroxides has been widely studied, as has the bacterial role in the formation of Si-Fe-Mn-oxyhydroxides (Emerson and Moyer, 2002; Emerson et al., 2007; Edwards et al., 2003; Kennedy et al., 2003; Fortin and Langley, 2005). However, there is less research concerning the formation conditions of Si-Fe-Mn-oxyhydroxides. This paper uses Pourbaix diagrams to explain the formation conditions of Si-Fe-Mn-oxyhydroxides at the PACMANUS hydrothermal field.

2 Geological setting

The Manus Basin is a young (ca. 3.5 Ma old) back-arc basin with a fast-spreading rate (up to 137 mm/a; Tregoning, 2002). It is bound by the Manus trench to the north and the New Britain Trench to the south (Taylor, 1979; Fig. 1a). Eastern Manus Basin (EMB) is located between the Djaul and Weitin transform faults (Martinez and Taylor, 1996; Fig. 1b).

Volcanism associated with an earlier rifting phase in the Eastern Manus Basin has produced a series of echelon volcanic ridges and volcanic cones (Eastern Manus volcanic zone; Binns and Scott, 1993; Sinton et al., 2003). The composition of lavas changes progressively from basaltic to rhyodacitic (Binns and Scott, 1993; Sinton et al., 2003). The Eastern Manus Basin

Foundation item: The National Key Basic Research Program of China under contract Nos 2013CB429700; the National Special Fund for the 12th Five Year Plan of COMRA under contract Nos DY125-12-R-02 and DY125-12-R-05; the National Natural Science Foundation of China under contract Nos 41325021, 40830849, 40976027 and 41476044; the Shandong Province Natural Science Foundation of China for Distinguished Young Scholars under contract Nos JQ200913; the Strategic Priority Research Program of the Chinese Academy of Sciences under contract No. XDA11030302; the CAS/SAFEA International Partnership Program for Creative Research Teams.
*Corresponding author, E-mail: zgzeng@qdio.ac.cn

has three main hydrothermal fields: PACMANUS (Papua New Guinea-Australia-Canada-Manus), Desmos, and SuSu Knolls (Fig. 1b).

The PACMANUS hydrothermal field is located on the crest of the Pual Ridge (Figs 1b and c), which is a northeast-trending volcanic structure 15 km in length, 1.5 km in width, and 1 600–1 700 m in depth (Binns and Scott, 1993). The stem of the Pual Ridge is mainly composed of dacite (Binns and Scott, 1993). Pillowed and lobate tubular flows of vesicular andesite dominate the deeper, northeast-sloping platform between the two arms of Pual Ridge. The rocks are mainly lobate basaltic andesites (Binns and Scott, 1993). Some hydrothermal deposits are located along the Pual Ridge and form the PACMANUS field. PACMANUS hydrothermal field is composed of four high-temperature hydrothermal sites (Roger's Ruins, Roman Ruins, Satanic Mills, and Tsukushi) and a low-temperature hydrothermal site (Snowcap; Binns et al., 2007; Fig. 1c).

3 Samples and methods

3.1 *Samples*

Si-Fe-Mn-oxyhydroxide samples were collected by dredging (starting point 3°43.0751′S, 151°40.4173′E; end point 3°43.3952′S, 151°40.8478′E, water depth of 1 780 to 1 800 m) during the cruise "KX08-973" of the R/V *Kexueyihao* in the PACMANUS hydrothermal field in 2008 (Fig. 1c).

We chose two large samples for this study (Fig. 2): (1) yellow precipitates with honeycomb-like texture and a small amount of loose black and yellow-green materials (Fig. 2a, Sample #1) and (2) yellow, loose and fragile precipitates with a small amount of black, yellow-green materials with acicular textures containing white filamentous structures on the surface (Fig. 2b, Sample #2). Sub-samples from each sample were separated to make polished sections for optical microscope observations and electron microprobe analyses. A small portion of Sample #1 was sampled using a stainless-steel spatula to make polished Section 1 (Fig. 3a). The sub-sample was solid with black and yellow materials interspersed. The sampling location is shown in the red box in Fig. 2a. A small portion of Sample #2 was also sampled using a stainless-steel spatula to make polished Section 2 (Fig. 4a). The sub-sample was mainly composed of yellow, red-brown materials, with white filamentous structures on the surface. The sampling location is shown in the red box in Fig. 2b.

X-ray diffraction analysis showed the samples were poorly crystallized and amorphous. The yellow materials were composed of opal-A (the distinctive broad peak centered on 0.4 nm) and goethite (a small, weak peak at 0.256 nm). The black materials were composed of birnessite (peaks at 0.725 and 0.244 nm), todorokite (peak at 0.96 nm), and vernadite. The yellow green materials were composed of birnessite, todorokite and

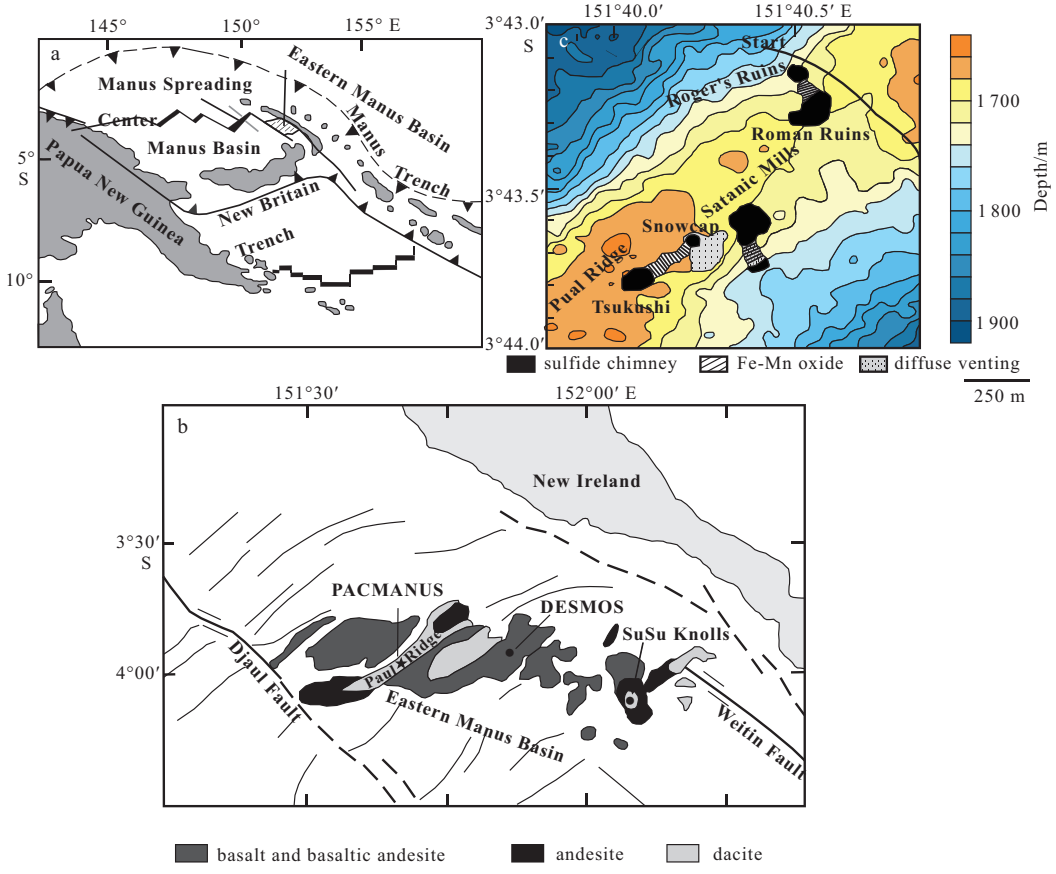

Fig.1. Tectonic setting and regional seafloor geology of the Eastern Manus Basin (a); locations of PACMANUS, Desmos, and SuSu Knolls hydrothermal fields on the East Manus Basin and the types of volcanic rocks (b); hydrothermal sites, hydrothermal deposit types and the dredge track (the black line nearby the Roger's Ruins and Roman Ruins) within the PACMANUS hydrothermal field (c) (modified after Binns et al., 2007).

nontronite (peaks at 1.54, 0.453 and 0.152 nm; Zeng et al., 2012).

The Si-Fe-Mn-oxyhydroxides had low concentrations of Ti and transition elements. The distribution patterns of rare earth elements had positive europium anomalies and slight light rare earth elements enrichment. In the Mn–Fe–(Co+Ni+Cu) ×10 ternary diagram, the samples were plotted in the hydrothermal-origin region. These geochemical characteristics of the samples suggest that the Si-Fe-Mn-oxyhydroxides directly precipitated from hydrothermal fluids (Zeng et al., 2012).

3.2 *Electron microprobe analysis*

Electron microprobe analysis was performed with a JXA-8230 electron microprobe operating at U=15 kV, I=2×10^{-8}A, with an electron beam diameter of 5 μm at the Institute of Mineral Resources, Chinese Academy of Geological Sciences. The standard materials were natural minerals or synthetic oxides of national standards.

3.3 *Thermodynamic modeling of Si-Fe-Mn-H_2O system*

3.3.1 *Thermodynamic data*

Since the vent fluids can mix with seawater, we used end-member compositions of the hydrothermal fluid to determine the true composition of the hydrothermal fluid. Reeves et al. (2011) used zero Mg concentration to obtain the composition of end-member fluid prior to mixing with seawater. The average values of total SiO_2, Fe, Mn and H_2S in the end-member hydrothermal fluids were 17.35 mmol/kg, 5.2 mmol/kg, 3.28 mmol/kg and 3.77 mmol/L, respectively (Reeves et al., 2011). In the thermodynamic modeling at 300°C, we chose $\sum SiO_2$ =17.35×10^{-3} mol/L, $\sum$Fe =5.20×10^{-3} mol/L, and $\sum$Mn = 3.28×10^{-3} mol/L. In the hydrothermal field, the deposition of iron sulfide minerals will result in the removal of Fe from the hydrothermal fluid. The report of ODP Leg 193 indicates that pyrite is the most disseminated sulfide (Binns et al., 2007). Therefore, the reaction of $Fe^{2+}+2H_2S=FeS_2+2H^++H_2$ is responsible for Fe removal. According to the average composition of total Fe and $\sum H_2S$ in the vent fluid and the reaction above, we calculated the amount of reactive (3.10 mmol/kg) and residual Fe (2.10 mmol/kg) in the hydrothermal fluid. Therefore, in the thermodynamic modeling at 25°C, we chose $\sum SiO_2$ =17.35×10^{-3} mol/L, $\sum$Fe = 2.10×10^{-3} mol/L, and $\sum$Mn = 3.28×10^{-3} mol/L. The pH of vent fluid at the Roger's Ruins and Roman Ruins fields ranged from 2.3 to 3.2, (Table 1), which overlaps with the lowest values (2.63–7.26) measured in 1995 (Fourre et al., 2006). The pH of the bottom seawater surrounding the PACMANUS hydrothermal field was 7.9. Therefore we chose 2.3 as the lower limit of pH and 7.9 as the upper limit of pH for our thermodynamic calculations. The temperature of vent fluid at the Roger's Ruins and Roman Ruins fields range from 272°C to 341°C (Reeves et al., 2011), with an average value of 297°C. As a matter of convenience, we chose 300°C as the high temperature for the thermodynamic calculations. Many studies have shown that the precipitation temperature of hydrothermal SiO_2 is 41.1–42.9°C (Sun et al., 2012), and hydrothermal Fe-Si-oxides are 3.6–20°C (Dekov et al., 2010). As a matter of convenience, we chose 25°C as the low temperature for the thermodynamic calculations.

Besides the chemistry parameters of the hydrothermal fluid, the Fe-oxyhydroxides and Mn-oxyhydroxides speciation and their standard free energies of formation must be selected for the thermodynamic modeling. There are some challenges in the selection process, namely the variety of Fe-oxyhydroxides and Mn-oxyhydroxides involved and the lack of chemical data on some species (Ponnamperuma et al., 1967).

Elemental Si is unstable relative to SiO_2. The dominant stable phase of Si in water is solid SiO_2. Dissolved species of $HSiO_3^-$ and $SiO_3(OH)^{3-}$ only appear under highly alkaline condi-

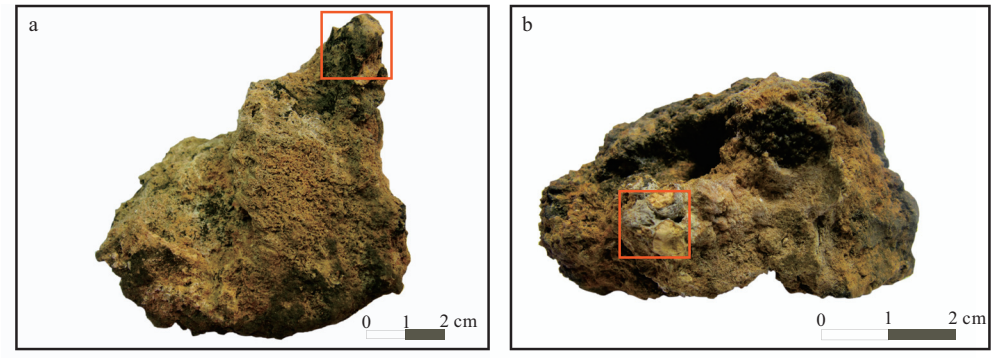

Fig.2. Photos of the Si-Fe-Mn-oxyhydroxides from PACMANUS hydrothermal field: a. Yellow precipitates with honeycomb-like texture (Sample #1), the red box is the sampling location of polished Section 1; b. loose yellow precipitates with white filaments on the surface (Sample #2), the red box is the sampling location of polished Section 2.

Table 1. Geochemistry of the end-member vent fluids from the PACMANUS hydrothermal field (Reeves et al., 2011)

	Roger's Ruins	Roman Ruins	Ambient seawater
T/°C	274–320	272–341	3
pH (at 25°C)	2.6–2.7	2.3–2.6	7.9
Fe/mmol·kg^{-1}	3.88–4.64	1.42–7.75	0
Mn/mmol·kg^{-1}	2.58–2.76	3.02–4.79	0
SiO_2/mmol·kg^{-1}	18.8–19	15.7–23.9	0.13
$\sum H_2S$/mmol·L^{-1}	2.8–3.6	4.0–7.5	0

tions (pH>10; Kim et al., 2012) which is higher than the typical pH of seawater (7.9). Therefore, Si and SiO_2 were chosen as the main species in the SiO_2-H_2O thermodynamic modeling and SiO_2 was used to represent opal-A in the Si-Fe-Mn-oxyhydroxide samples.

Fe has a wide range of oxidation states: –2 to +4. In acidic solutions, Fe forms Fe^{2+} and Fe^{3+}. Fe^{2+} hydrolyses to $FeOH^+$ and $Fe(OH)_2$(aq) and precipitates to $Fe(OH)_2$(s) when the pH rises to neutral. Fe^{3+} may hydrolyze to polynuclear complexes with increasing pH (Beverskog and Puigdomenech, 1996). In soils, $Fe(OH)_3{\cdot}nH_2O$ is regarded as the main species, whereas the reduction products of Fe^{3+} may be $Fe_3(OH)_8$ or $Fe_4(OH)_{10}$ (Ponnamperuma et al., 1967). $Fe_3(OH)_8$ is named ferrosic hydroxide, which is a compound formed by mixing $Fe(OH)_2$ and $Fe(OH)_3$ (Ponnamperuma et al., 1967; Schwab et al., 1983; Boyd and Scott, 2001). Therefore we chose Fe^{2+}, Fe^{3+}, $Fe(OH)_2$, and $Fe(OH)_3$ as the primary species in the Fe-H_2O thermodynamic modeling. We chose $Fe(OH)_3$ to represent ferric hydroxide (goethite) in the Si-Fe-Mn-oxyhydroxide samples and chose $Fe_3(OH)_8$ to represent the unstable precursor of magnetite.

There are many factors influencing the speciation of Mn oxides, of which pH may be the most important (Ponnamperuma et al., 1969). Based on the pH range of PACMANUS hydrothermal fluid and that of the ambient seawater, we chose species of Mn oxides which are stable at pH values of 2.3 to 7.9. Ponnamperuma et al. (1969) reported the pH range of δ-MnO_2, γ-MnO_2, γ-Mn_2O_3, γ-MnOOH, and Mn_3O_4 are 3.7–4.2, 4.2–4.6, 6.5–7.2, 6.4–7.0 and 6.3–6.9, respectively. Therefore, we chose MnO_2, Mn_2O_3, MnOOH, and Mn_3O_4 as the primary species in the Mn-H_2O thermodynamic modeling. We chose MnO_2 to represent vernadite and chose Mn_2O_3 to represent amorphous birnessite (Wang et al., 2009) in the Si-Fe-Mn-oxyhydroxide samples. The standard molar Gibbs free energies of formation for Fe and Mn oxides species were obtained from previous works (Sadiq and Lindsay, 1979; Lin et al., 1985).

Table 2 is a compilation of the thermodynamic data used for the modeling in the PACMANUS hydrothermal field. Table 3 presents the equations of the Si-Fe-Mn-H_2O systems.

3.3.2 *Calculations*

Table 2. Standard Gibbs free energy of formation of species at 25°C for the Si-Fe-Mn-H_2O system

	$\Delta_f G^\theta$/kcal·mol^{-1}	$\Delta_f G^\theta$/kJ·mol^{-1}
SiO_2	–203.020 (Sadiq and Lindsay, 1979)	–849.811
Fe^{3+}(aq)	–4.020 (Sadiq and Lindsay, 1979)	–16.827
Fe^{2+}(aq)	–21.800 (Sadiq and Lindsay, 1979)	–91.252
$Fe(OH)_2$(s)	–117.584 (Sadiq and Lindsay, 1979)	–492.189
$Fe(OH)_3$(s)	–169.250 (Sadiq and Lindsay, 1979)	–708.455
$Fe_3(OH)_8$(s)	–459.220 (Sadiq and Lindsay, 1979)	–1922.226
H_2O	–56.687 (Sadiq and Lindsay, 1979)	–237.283
Mn^{2+}	–54.908	–229.840 (Lin et al., 1985)
MnO_2	–111.106	–465.075 (Lin et al., 1985)
Mn_2O_3	–210.150	–879.658 (Lin et al., 1985)
Mn_3O_4	–305.976	–1280.771 (Lin et al., 1985)
$Mn(OH)_2$	–147.309	–616.614 (Lin et al., 1985)

Table 3. Equations for the Si-Fe-Mn-H_2O system

Chemical equations	T=573.15 K	T=298.15 K
(1) $Fe^{3+}+e=Fe^{2+}$	Φ=0.771	Φ=0.771
(2) $Fe^{2+}+2e=Fe$	Φ=–0.603	Φ=–0.552
(3) $Fe^{2+}+2H_2O=Fe(OH)_2+2H^+$	pH=4.5	pH=7.79
(4) $Fe^{3+}+3H_2O=Fe(OH)_3+3H^+$	pH=1.376	pH=2.07
(5) $Fe(OH)_3+3H^++e=Fe^{2+}+3H_2O$	Φ=1.24–0.341 pH	Φ=1.138–0.178 pH
(6) $3Fe(OH)_3+H^++e=Fe_3(OH)_8+H_2O$	Φ=0.354–0.114 pH	Φ=0.353–0.059 pH
(7) $Fe_3(OH)_8+8H^++2e=3Fe^{2+}+8H_2O$	Φ=1.683–0.454 pH	Φ=1.532–0.237 pH
(8) $Fe_3(OH)_8+2H^++2e=3Fe(OH)_2+2H_2O$	Φ=0.150–0.114 pH	Φ=0.150–0.059 pH
(9) $Fe(OH)_2+2H^++2e=Fe+2H_2O$	Φ=–0.091–0.114 pH	Φ=–0.091–0.059 pH
(10) $Mn^{2+}+2e=Mn$	Φ=–1.332	Φ=–1.264
(11) $Mn^{2+}+2H_2O=Mn(OH)_2+2H^+$	pH=5.24	pH=8.93
(12) $MnO_2+4H^++2e=Mn^{2+}+2H_2O$	Φ=1.381–0.227 pH	Φ=1.313–0.118 pH
(13) $2MnO_2+2H^++2e=Mn_2O_3+H_2O$	Φ=0.968–0.114 pH	Φ=0.968–0.059 pH
(14) $Mn_2O_3+6H^++2e=2Mn^{2+}+3H_2O$	Φ=1.795–0.341 pH	Φ=1.66–0.178 pH
(15) $3Mn_2O_3+2H^++2e=2Mn_3O_4+H_2O$	Φ=0.828–0.114 pH	Φ=0.828–0.059 pH
(16) $Mn_3O_4+8H^++2e=3Mn^{2+}+4H_2O$	Φ=2.278–0.455 pH	Φ=2.075–0.237 pH
(17) $Mn(OH)_2+2H^++2e=Mn+2H_2O$	Φ=–0.736–0.114 pH	Φ=–0.736–0.059 pH
(18) $Mn_3O_4+2H_2O+2H^++2e=3Mn(OH)_2$	Φ=0.49–0.114 pH	Φ=0.49–0.059 pH
(19) $SiO_2+4H^++4e=Si+2H_2O$	Φ=–1.026–0.114 pH	Φ=–1–0.059 pH
(20) $O_2+4H^++4e=2H_2O$	Φ=1.23–0.114 pH	Φ=1.23–0.059 pH
(21) $2H^++2e=H_2$	Φ=–0.114 pH	Φ=–0.059 pH

The possible chemical reactions in the Si-Fe-Mn-H_2O system can be divided into three types:

(1) Reactions related only to the electrode potential, that are independent of pH (horizontal solid lines in the Pourbaix diagrams of Figs 5 and 6). The equation is

$$aA + bB + ne = cC + dD\ ;$$

the formula is

$$\phi = -\frac{\Delta_r G^{\theta}_{298.15}}{nF} + \frac{2.303RT}{nF}\lg\frac{\alpha A^a \alpha B^b}{\alpha C^c \alpha D^d}\ ,$$

where A and B are reactants, C and D are products, a, b, c, and d are the stoichiometric coefficient of chemical reactions, e is electron, n is the number of moles of electrons transferred in the reaction, α is activity of species, ϕ is the electrode potential, $\Delta_r G^{\theta}_{298.15}$ is the standard change of reaction in Gibbs free energy, R is the gas constant (8.3144 J/(K·mol)), T is absolute temperature (573.15 K), and F is the Faraday constant (96.487 kJ/(V·mol)).

(2) Reactions related only to pH, but not to electrode potential (vertical solid lines in the Pourbaix diagrams of Figs 5 and 6). The formula is

$$\Delta_r G^{\theta}_{298.15} = -RT\ln K\ ,$$

where K is the equilibrium constant.

(3) Reactions related to both pH value and electrode potential (sloping solid lines in the Pourbaix diagrams of Figs 5 and 6). The equation is

$$aA + bB + ne + hH^+ = cC + dD\ ;$$

the formula is

$$\phi = -\frac{\Delta_r G^{\theta}_{298.15}}{nF} + \frac{2.303RT}{nF}(\lg\frac{\alpha A^a \alpha B^b}{\alpha C^c \alpha D^d} - h\cdot pH)\ .$$

The chemical parameters (Tables 1 and 2) and chemical reactions (Table 3) were entered into the origin software to create the initial Pourbaix diagrams which were further modified using CorelDraw.

4 Results

4.1 *Microscopic textures*

The two hydrothermal precipitate samples had different textures. Polished Section 1 had an obvious nuclei with concentric layers of different colors (Fig. 3a). Polished Section 2 had large (hundreds of micrometers) ellipsoidal particles with red and yellow zonal texture (Fig. 4).

4.2 *Electron microprobe analysis*

The line scanning analysis (Fig. 3b) revealed that the composition of concentric nuclei varied from the edge to the core. The outermost layer (Layer I) had a high Fe content and minor amounts of Si. In the inner layer (Layer II), the content of Si increased gradually, the content of Mn was lower than in Layer I, but with no variation, and the content of Fe decreased sharply from Layer I to II. In the second inner layer (Layer III), the content of Si decreased sharply, while the content of Mn increased sharply compared with Layer I and II and reached a maximum concentration. The core (Layer IV), contained the highest content of Si, whereas the content of Mn decreased to aminimum. Overall, in the whole concentric nucleus, the changes of Si and Mn showed opposite trends, while the content of Fe reached its highest value in the outermost layer and was much lower in the other layers.

The areal scanning analysis (Figs 4c and d) showed that the large ellipsoidal grains mainly contained Si and Fe. The cores of the grains mainly contained Si with a small amount of Fe distributed in a zonal structure. In the outer part, the grains mostly contained Fe.

4.3 *Thermodynamics analysis*

The Si-Fe-Mn-H_2O systems are shown in Figs 5 and 6. Figures 5a and c show the Eh-pH diagrams for the Si-Fe-H_2O and Mn-H_2O systems at 573.15 K (300°C), respectively. Figures 5b and d show the Eh-pH diagrams for the Si-Fe-H_2O and Mn-H_2O systems at 298.15 K (25°C), respectively. Figures 6a and b present the integrated Eh-pH diagrams for the Si-Fe-Mn-H_2O system at 573.15 K and 298.15 K, respectively. In Figs 5 and 6, the sloping dotted lines represent the stability boundaries of H_2-H_2O and H_2O-O_2 and the vertical dotted lines represent the lower limit of pH (pH=2.3) of the hydrothermal fluid and the upper limit of pH (pH=7.9) of the bottom seawater around the sampling hy-

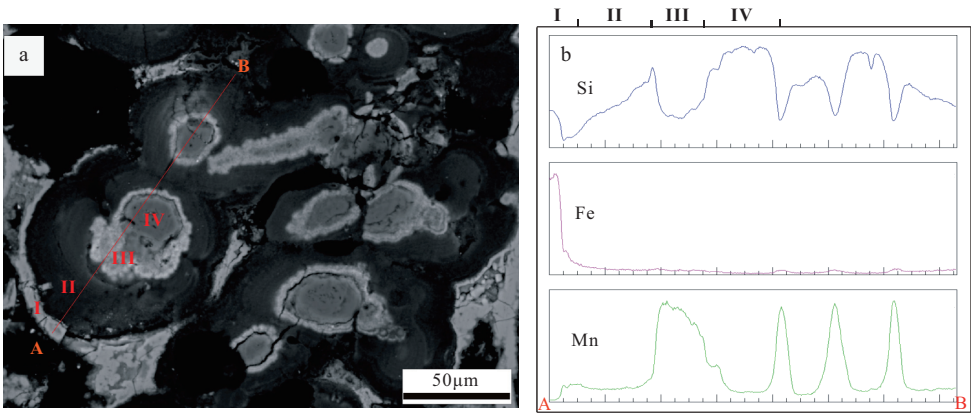

Fig.3. Back-scattered electrons image of polished Section 1 (a) and line scanning analysis along Transect A and B of polished Section 1 (b).

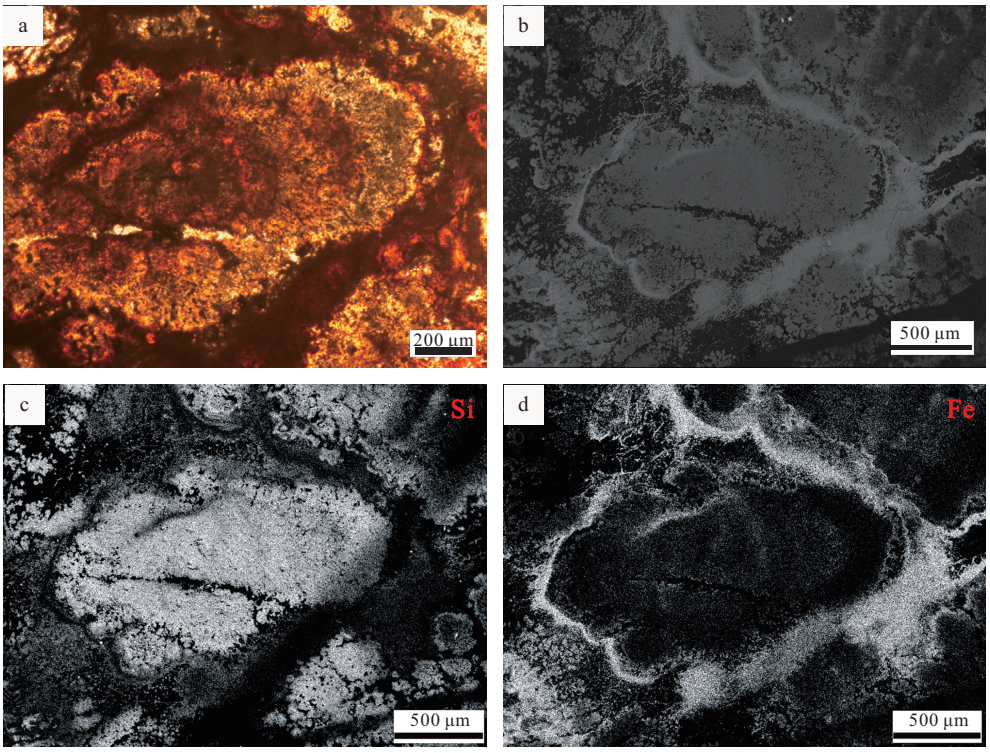

Fig.4. Photomicrograph (optical microscope with plane polarized light) of polished Section 2 (a), back-scattered electrons image of polished Section 2 (b); and areal scanning analysis of polished Section 2 (c and d).

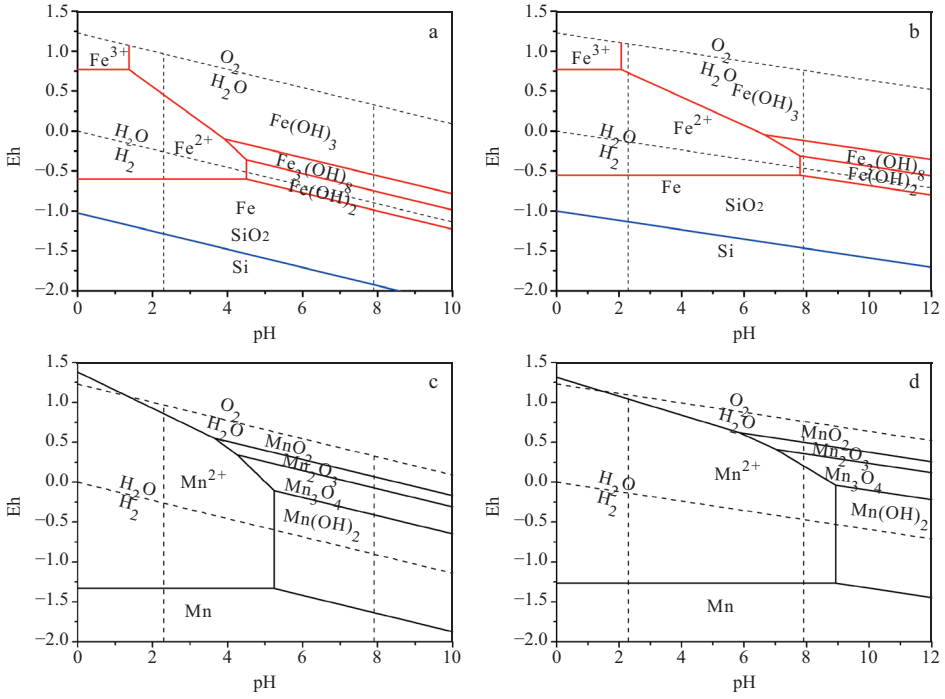

Fig.5. Eh-pH diagram for the Si-Fe-H_2O system at 300°C (a); Eh-pH diagram for the Si-Fe-H_2O system at 25°C (b); Eh-pH diagram for the Mn-H_2O system at 300°C (c); and Eh-pH diagram for the Mn-H_2O system at 25°C (d). Sloping dotted lines represent the stability boundaries of H_2-H_2O and H_2O-O_2. Vertical dotted lines represent the lower limit of pH value (pH=2.3) of the hydrothermal fluid and the pH value of ambient seawater (pH=7.9). The blue, red and black solid lines represent the stability boundaries of Si, Fe and Mn, respectively.

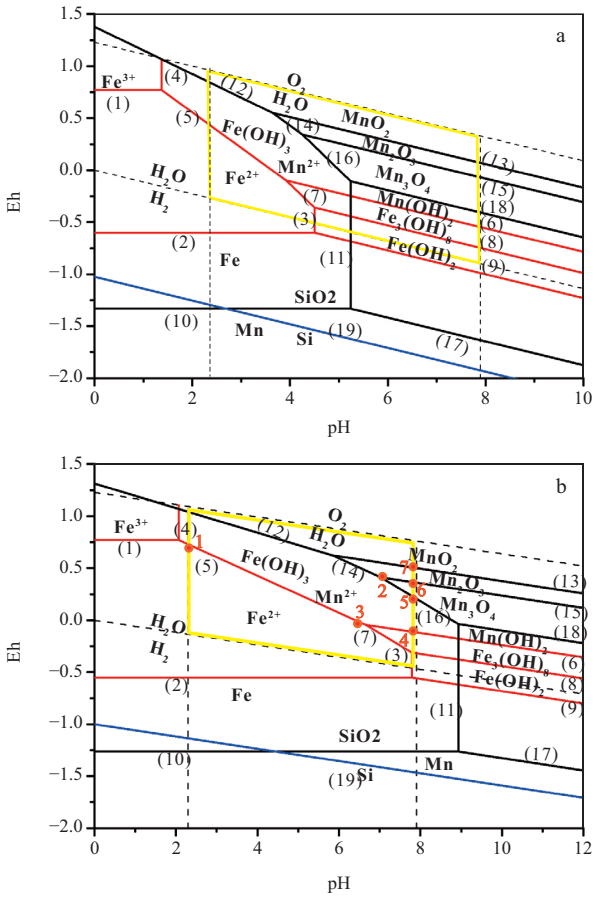

Fig.6. Integrated Eh-pH diagram for the Si-Fe-Mn-H_2O system at 300°C (a) and integrated Eh-pH diagram for the Si-Fe-Mn-H_2O system at 25°C (b). Yellow quadrilaterals represent the range of pH-Eh values at the sampling sites. Sloping dotted lines represent the stability boundaries of H_2-H_2O and H_2O-O_2. Vertical dotted lines represent the lower limit of pH value (pH=2.3) of the hydrothermal fluid and the pH value of ambient seawater (pH=7.9). Blue, red and black solid lines represent the stability boundaries of Si, Fe and Mn, respectively.

drothermal vents. The blue, red, and black solid lines represent the stability boundaries of Si, Fe and Mn, respectively.

The stability region of SiO_2 (Figs 6a and b) is constrained by Line 19. The stability region of Fe^{2+} (Figs 6a and b) is constrained by Lines 1, 2, 3, 5, and 7, and the stability region of Mn^{2+} is constrained by Lines 10, 11, 12, 14, and 16. Figures 5 and 6 show that Si is easily oxidized to SiO_2 above –1 V at pH 0. This Eh value is far below the water stability boundary. Figures 5 and 6 also show that SiO_2 precipitates significantly earlier than Fe-Mn-oxyhydroxides.

In the Pourbaix diagrams (Figs 5 and 6), the stability field of Mn^{2+} is larger than that of Fe^{2+}. The Mn^{2+} oxidation requires a higher Eh and pH than Fe^{2+}.

The yellow quadrilaterals in Figs 6a and b represent the range of Eh-pH at the sampling sites. The yellow quadrilateral in Fig. 6a represents the high-temperature conditions (300°C) before the mixing of hydrothermal fluid with seawater and the yellow quadrilateral in Fig. 6b represents the low-temperature conditions (25°C) after mixing of hydrothermal fluid with seawater. Compared with Fig. 6a, the amounts and kinds of Fe-Mn-oxyhydroxides in the region enclosed by the yellow quadrilateral decrease in Fig. 6b.

5 Discussion

5.1 *Pourbaix diagrams help decipher the precipitation conditions of the Si-Fe-Mn-oxyhydroxides*

Pourbaix diagrams have been widely used to explain the geological processes associated with fluids. Pourbaix diagrams can show the stability field of a particular element in a specific environment.

The Eh value of normal seawater is close to 0.4 (Silver, 1991) and mainly controlled by the oxygen system (Cooper, 1937). The hydrothermal fluids of Roger's Ruins and Roman Ruins are hot (272–341°C), acidic (pH of 2.3–3.2), and reduced (Table 1). Therefore, the Eh-pH values of the initial hydrothermal fluid should be located in the bottom left of the yellow quadrilateral at low pH and Eh values in Fig. 6a. When hydrothermal fluid mixes with seawater, the pH and Eh values of the hydrothermal fluid increase and oxyhydroxides will begin to precipitate. The conditions of the hydrothermal fluid will migrate towards the upper right corner in the yellow quadrilateral (Fig. 6a). At the same time, the temperature of hydrothermal fluid will drop. Figure 6b is the Si-Fe-Mn-H_2O Pourbaix diagram at 25°C.

The stability boundary (Line 19) of SiO_2 is far below stability boundaries (Lines 3, 4, 5, 7, 9, 11, 12, 14, 16, 17) of Fe-Mn-oxyhydroxides which indicate SiO_2 will precipitate earlier than Fe-Mn-oxyhydroxides.

Assuming the pH value of hydrothermal fluid is close to 7.9 when the Fe-Mn-oxyhydroxides precipitate and the Eh value increases from reducing conditions to 0.4 (the value of normal seawater), $Fe(OH)_2$ will precipitate first, followed by $Fe_3(OH)_8$ and $Fe(OH)_3$, and then a small portion of Mn_3O_4 and Mn_2O_3 will precipitate. If the pH and Eh of the hydrothermal fluid is lower than 0.742 5 and 0.4 (Point 2 in Fig. 6b), respectively, the only product will be $Fe(OH)_3$.

The stability field of Mn^{2+} is larger than that of Fe^{2+} (Figs 6a and b), which indicates that Mn^{2+} will remain in the fluid at a wider range of Eh-pH values. The hydrothermal fluid is acidic, reduced, and hot. As hydrothermal fluid mixes with seawater, the pH and Eh of the hydrothermal fluid increases. Fe-oxyhydroxides will precipitate first and as pH and Eh increase further, Mn-oxyhydroxides will subsequently precipitate.

A small amount of $Fe(OH)_2$ appeared in the lower right corner of the yellow quadrilateral (Fig. 6b), which indicates $Fe(OH)_2$ is stable at high pH and low Eh. Figure 6b shows that $Fe(OH)_2$ is not a major oxide species and it will disappear rapidly when Eh increases.

$Fe(OH)_3$ is a dominate species in all Fe oxides, and can form at a wide range of pH values (Figs 5a and b). When the pH of hydrothermal fluid is close to 2.3 (the lowest pH value of the PACMANUS hydrothermal fluid), the precipitation of $Fe(OH)_3$ requires a higher Eh up to 0.73 (Point 1 in Fig. 6b). However, this value is far from the normal seawater Eh (0.4). Therefore, $Fe(OH)_3$ could not precipitate in a condition of low pH and high Eh. When the pH of the hydrothermal fluid is close to 7.9 (pH of seawater), $Fe(OH)_3$ can precipitate at a lower Eh of –0.114 V (Point 4 in Fig. 6b). This indicates $Fe(OH)_3$ is easily deposited in

alkaline solution with little influence from Eh.

The ability of $Fe_3(OH)_8$ to form at a narrow range of Eh (<–0.044; Point 3 in Fig. 6b) and at higher pH indicates $Fe_3(OH)_8$ is stable in a reducing and alkaline environment. However, when hydrothermal fluid mixes with seawater completely, it becomes an oxidizing environment. Therefore, $Fe_3(OH)_8$ may form before hydrothermal fluid and seawater mix completely.

The lowest Eh for the formation of Mn_3O_4 is 0.205 (Point 5 in Fig. 6b); however, the precipitation of Mn_2O_3 requires an Eh value greater than 0.361 (Point 6 in Fig. 6b), which indicates Mn_3O_4 will precipitate before Mn_2O_3. Of all Mn oxides, MnO_2 has the largest field of stability in the Pourbaix diagrams (Fig. 6). But whatever the pH value is, the precipitation of MnO_2 requires high Eh values. The lowest possible Eh value for the precipitation of MnO_2 is 0.5 when the pH is close to 7.9 (Point 7 in Fig. 6b). However, the Eh of normal seawater is close to 0.4 (Silver, 1991). Therefore, at a temperature of 25°C and $\sum Mn=3.28\times10^{-3}$ mol/L, it is difficult to form MnO_2.

5.2 *Physical-chemical conditions for the formation of Si-Fe-Mn-concentric particles*

The back-scattered electrons image and line scanning analysis (Fig. 3) showed that the concentric nucleus was rich in Si and Mn with a small amount of Fe on the edge. The distribution of Si and Mn showed that Si oxide formed first in the core and Mn oxide formed subsequently around the Si core. Then the hydrothermal fluid shifted to become rich in Si and Fe and precipitated another layer of Si and Fe around the Si-Mn core. The photomicrograph and areal scanning analysis (Fig. 4) showed that the core of the large ellipsoid was mainly composed of Si with a small amount of Fe, whereas the edge mainly contained Fe. The distribution of Si and Fe indicates Si oxide precipitated first with a small amount of Fe oxide precipitating at the same time. Then large amounts of Fe oxide precipitated around the Si core.

As discussed above, Si is mainly distributed in the core of the concentric nucleus (Fig. 3) and ellipsoid (Fig. 4), while Fe and Mn are distributed on the edge. This indicates Si oxide precipitated earlier than Fe, Mn oxides. The Pourbaix diagrams (Figs 5 and 6) also show that the stability boundaries of SiO_2 (Line 19) are lower than Fe-Mn-oxyhydroxides. This also indicates SiO_2 precipitated first in the Si-Fe-Mn-oxyhydroxides (Lines 3, 5, 7, 9, 12, 14, 16, and 18).

The solubility of SiO_2 increases with temperature, pressure, and pH (White et al., 1956; Rimstidt and Cole, 1983). In the early period of precipitation, the hydrothermal fluid was hot and acidic, therefore the solution was undersaturated in SiO_2. When hydrothermal fluid encountered seawater, the temperature abruptly fell. The lower temperature and increasing pH promoted the precipitation of SiO_2. The complete mixing of hydrothermal fluid with seawater diluted the concentration of SiO_2 in the solution. Therefore, SiO_2 in the concentric nucleus (Fig. 3) and ellipsoid (Fig. 4) may have precipitated before hydrothermal fluid mixed with seawater.

After the precipitation of SiO_2 in the core (Fig. 3), the rising hydrothermal fluid mixed with seawater which increased the pH and Eh. This condition promoted the precipitation of Mn oxides around the Si oxides (Fig. 6b). The Fe oxyhydroxides in the outermost layer may indicate the composition of the hydrothermal fluid changed on a micrometer scale, because Fe oxyhydroxides cannot precipitate after Mn oxyhydroxides.

In the large ellipsoid (Fig. 4), the core mainly contained Si with a small amount of Fe, whereas the edge mainly contained Fe. In the early stages of formation, SiO_2 precipitated first from the hydrothermal fluid before mixing with seawater, as discussed above. At this time, the pH and Eh of the hydrothermal fluid increased gradually, but remained acidic. The Eh-pH values of the hydrothermal fluid are then located on the left side of yellow quadrilateral (Fig. 6b). If the Eh is high enough to exceed the equilibrium line of Fe^{2+} and $Fe(OH)_3$ (Line 5), a small amount of $Fe(OH)_3$ will precipitate in the Si-rich core. This may explain the occurrence of a small amount of Fe in the core. In the later period of formation, as discussed in Section 5.1, $Fe(OH)_3$ was easily deposited in an alkaline solution with little influence by Eh. After the complete mixture of the hydrothermal fluid with seawater, the hydrothermal fluid is close to neutral or slightly alkaline and $Fe(OH)_3$ was easily precipitated from solution (as discussed in Section 5.1) and distributed around the Si-rich core.

6 Conclusions

(1) According to the Si, Fe and Mn concentrations in the end-member PACMANUS hydrothermal fluid, we created Si-Fe-Mn-H_2O Pourbaix diagrams at 300°C and 25°C. Si-Fe-Mn-H_2O Pourbaix diagrams showed that the main Si, Fe and Mn oxides species were SiO_2, $Fe(OH)_3$, $Fe_3(OH)_8$, Mn_3O_4, and Mn_2O_3 at 25°C. In the mixing process of hydrothermal fluid with seawater, SiO_2 precipitated earlier than Fe-Mn-oxyhydroxides because of the lower stability boundary. Then $Fe(OH)_2$ precipitated first, followed by $Fe_3(OH)_8$ and $Fe(OH)_3$, and last, small amounts of Mn_3O_4 and Mn_2O_3 precipitated. $Fe(OH)_3$ was easily deposited in the alkaline solution with little influence by Eh. $Fe_3(OH)_8$ was readily formed before the complete mixture of hydrothermal fluid with seawater. Mn_3O_4 precipitated before Mn_2O_3.

(2) In the concentric nucleus and ellipsoid, Si oxides precipitated first before hydrothermal fluid mixed with seawater. In the concentric nucleus, after the precipitation of SiO_2, the increase of pH and Eh promoted the precipitation of Mn oxides around the Si oxides. In the large ellipsoid, the precipitation of Fe oxides was divided into two periods. In the early period, SiO_2 precipitated first before mixing with seawater. The cool and acidic hydrothermal fluid promoted the precipitation of a small amount of $Fe(OH)_3$ in the Si-rich core. In the late period, after complete mixture of hydrothermal fluid and seawater, the hydrothermal fluid was close to neutral or slightly alkaline, and $Fe(OH)_3$ was readily precipitated from the solution and distributed around the Si-rich core.

Acknowledgements

We are sincerely grateful for the constructive and helpful comments provided by two anoymous reviewers. We are also thankful to the crew for their help with obtaining the samples during the "KX08-973" cruise.

References

Alt J C. 1988. Hydrothermal oxide and nontronite deposits on seamounts in the eastern Pacific. Mar Geol, 81(1–4): 227–239

Benjamin S B, Haymon R M. 2006. Hydrothermal mineral deposits and fossil biota from a young (0. 1 Ma) abyssal hill on the flank of the fast spreading East Pacific Rise: Evidence for pulsed hydrothermal flow and tectonic tapping of axial heat and fluids. Geochem-

istry Geophysics Geosystems, 7(5): Q05002
Beverskog B, Puigdomenech I. 1996. Revised Pourbaix diagrams for iron at 25–300°C. Corros Sci, 38(12): 2121–2135
Binns R A, Scott S D. 1993. Actively forming polymetallic sulfide deposits associated with felsic volcanic rocks in the eastern Manus back-arc basin, Papua New Guinea. Econ Geol, 88(8): 2226–2236
Binns R A, Scott S D, Bogdanov Y A, et al. 1993. Hydrothermal oxide and gold-rich sulfate deposits of Franklin Seamount, western Woodlark Basin, Papua New Guinea. Econ Geol, 88(8): 2122–2153
Binns R A, Barriga F J A S, Miller D J. 2007. 1. Leg 193 Synthesis: Anatomy of an active felsic-hosted hydrothermal system, eastern Manus Basin, Papua New Guinea. Proceedings of the Ocean Drilling Program, Scientific Results, 193: 1–71
Bogdanov Y A, Lisitzin A P, Binns R A, et al. 1997. Low-temperature hydrothermal deposits of Franklin Seamount, Woodlark Basin, Papua New Guinea. Mar Geol, 142(1–4): 99–117
Bonatti E, Beyth M, Rydell H S, et al. 1972. Iron-manganese-barium deposit from the northern Afar Rift (Ethiopia). Econ Geol, 67(6): 717–730
Boyd T D, Scott S D. 2001. Microbial and hydrothermal aspects of ferric oxyhydroxides and ferrosic hydroxides: the example of Franklin Seamount, Western Woodlark Basin, Papua New Guinea. Geochem T, 2(1): 45–56
Cooper L H N. 1937. Oxidation-reduction potential in sea water. J Mar Biol Assoc UK, 22(1): 167–176
Dekov V M, Petersen S, Garbe-Schonberg C D, et al. 2010. Fe-Si-oxyhydroxide deposits at a slow-spreading centre with thickened oceanic crust: The Lilliput hydrothermal field (9°33'S, Mid-Atlantic Ridge). Chem Geol, 278(3–4): 186–200
Edwards K J, Glazer B, Rouxel O J, et al. 2011. Ultra-diffuse hydrothermal venting supports Fe-oxidizing bacteria and massive umber deposition at 5000 m off Hawaii. The ISME Journal, 5(11): 1748–1758
Edwards K J, Rogers D R, Wirsen C O, et al. 2003. Isolation and characterization of novel psychrophilic, neutrophilic, Fe-oxidizing, chemolithoautotrophic α- and γ-Proteobacteria from the deep sea. Appl Environ Microb, 69(5): 2906–2913
Emerson D, Moyer C L. 2002. Neutrophilic Fe-oxidizing bacteria are abundant at the Loihi Seamount hydrothermal vents and play a major role in Fe oxide deposition. Appl Environ Microb, 68(6): 3085–3093
Emerson D, Rentz J A, Lilburn T G, et al. 2007. A novel lineage of proteobacteria involved in formation of marine Fe-oxidizing microbial mat communities. Plos One, 2(8): e667
Fortin D, Langley S. 2005. Formation and occurrence of biogenic iron-rich minerals. Earth-Sci Rev, 72(1–2): 1–19
Fourre E, Jean-Baptiste P, Charlou J L, et al. 2006. Helium isotopic composition of hydrothermal fluids from the Manus back-arc Basin, Papua New Guinea. Geochem J, 40(3): 245–252
Halbach P D P. 1986. Processes controlling the heavy metal distribution in Pacific ferromanganese nodules and crusts. Geologische Rundschau, 75(1): 235–247
Hein J R, Hsueh-Wen Y, Gunn S H, et al. 1994. Composition and origin of hydrothermal ironstones from central Pacific seamounts. Geochim Cosmochim Ac, 58(1): 179–189
Hein J R, Koschinsky A, Halbach P, et al. 1997. Iron and manganese oxide mineralization in the Pacific. Manganese Mineralization: Geochemistry and Mineralogy of Terrestrial and Marine Deposits, 119(16): 123–138
Hein J R, Schulz M S, Dunham R E, et al. 2008. Diffuse flow hydrothermal manganese mineralization along the active Mariana and southern Izu-Bonin arc system, western Pacific. J Geophys Res, 113(B8): B08S14
Hekinian R, Hoffert M, Larque P, et al. 1993. Hydrothermal Fe and Si oxyhydroxide deposits from south Pacific intraplate volcanoes and east Pacific rise axial and offaxial regions. Economic Geology and the Bulletin of the Society of Economic Geologists, 88: 2099–2121
Hrischeva E, Scott S D. 2007. Geochemistry and morphology of metalliferous sediments and oxyhydroxides from the Endeavour segment, Juan de Fuca Ridge. Geochim Cosmochim Ac, 71(14): 3476–3497
Iizasa K, Kawasaki K, Maeda K, et al. 1998. Hydrothermal sulfide-bearing Fe-Si oxyhydroxide deposits from the Coriolis Troughs, Vanuatu backarc, southwestern Pacific. Mar Geol, 145(1–2): 1–21
Karl D M, Brittain A M, Tilbrook B D. 1989. Hydrothermal and microbial processes at Loihi Seamount, a mid-plate hot-spot volcano. Deep-Sea Research Part A: Oceanographic Research Papers, 36(11): 1655–1673
Kennedy C B, Scott S D, Ferris F G. 2003. Characterization of bacteriogenic iron oxide deposits from Axial Volcano, Juan de Fuca Ridge, northeast Pacific Ocean. Geomicrobiol J, 20(3): 199–214
Kim E, Osseo-Asare K. 2012. Dissolution windows for hydrometallurgical purification of metallurgical-grade silicon to solar-grade silicon: Eh–pH diagrams for Fe silicides. Hydrometallurgy, 127–128: 178–186
Lin Chuanxian, Bai Zhenghua, Zhang Zheru. 1985. Thermodynamic Data Handbook of Minerals and Related Compounds (in Chinese). Beijing: Science Press, 17
Little C T S, Glynn S E J, Mills R A. 2004. Four-hundred-and-ninety-million-year record of bacteriogenic iron oxide precipitation at sea-floor hydrothermal vents. Geomicrobiol J, 21(6): 415–429
Martinez F, Taylor B. 1996. Backarc spreading, rifting, and microplate rotation, between transform faults in the Manus Basin. Marine Geophysical Researches, 18(2–4): 203–224
Ponnamperuma F N, Loy T A, Tianco E M. 1969. Redox equilibria in flooded soils: II. The manganese oxide systems. Soil Sci, 108(1): 48–57
Ponnamperuma F N, Tianco E M, Loy T. 1967. Redox equilibria in flooded soils: I. The iron hydroxide systems. Soil Sci, 103(6): 374–382
Reeves E P, Seewald J S, Saccocia P, et al. 2011. Geochemistry of hydrothermal fluids from the PACMANUS, Northeast Pual and Vienna Woods hydrothermal fields, Manus Basin, Papua New Guinea. Geochim Cosmochim Ac, 75(4): 1088–1123
Rimstidt J D, Cole D R. 1983. Geothermal mineralization: I. The mechanism of formation of the Beowawe, Nevada, siliceous sinter deposit. Am J Sci, 283(8): 861–875
Sadiq M, Lindsay W L. 1979. Selection of standard free energies of formation for use in soil chemistry. Technical Bulletin/Colorado State University, Experiment Station, 134: 1–24
Schwab A P, Lindsay W L. 1983. Effect of redox on the solubility and availability of iron. Soil Sci Soc Am J, 47: 201–205
Silver G L. 1991. Environmental plutonium: What is the redox potential of seawater? J Radioanal Nucl Ch, 155(3): 177–181
Sinton J M, Ford L L, Chappell B, et al. 2003. Magma genesis and mantle heterogeneity in the Manus Back-Arc Basin, Papua New Guinea. J Petrol, 44(1): 159–195
Sun Zhilei, Zhou Huaiyang, Glasby G P, et al. 2012. Formation of Fe–Mn–Si oxide and nontronite deposits in hydrothermal fields on the Valu Fa Ridge, Lau Basin. J Asian Earth Sci, 43(1): 64–76
Takahashi Y, Manceau A, Geoffroy N, et al. 2007. Chemical and structural control of the partitioning of Co, Ce, and Pb in marine ferromanganese oxides. Geochim Cosmochim Ac, 71(4): 984–1008
Taylor B. 1979. Bismarck Sea: Evolution of a back-arc basin. Geology, 7(4): 171–174
Tregoning P. 2002. Plate kinematics in the western Pacific derived from geodetic observations. Journal of Geophysical Research: Solid Earth, 107(B1): ECV 7–1–ECV 7–8
Wang Yuan, Chai Ruitao, Li Nan, et al. 2009. Synthesis of birnessite. Journal of Jilin University (Science Edition) (in Chinese), 47(3): 614–617
White D E, Brannock W W, Murata K J. 1956. Silica in hot-spring waters. Geochim Cosmochim Ac, 10(1–2): 27–59
Zeng Zhigang, Ouyang Hegen, Yin Xuebo, et al. 2012. Formation of Fe-Si-Mn oxyhydroxides at the PACMANUS hydrothermal field, Eastern Manus Basin: mineralogical and geochemical evidence. J Asian Earth Sci, 60: 130–146